

Optimal charge-to-spin conversion in graphene on transition metal dichalcogenides

Manuel Offidani,¹ Mirco Milletari,^{2,3,*} Roberto Raimondi,² and Aires Ferreira^{1,†}

¹*Department of Physics, University of York, York YO10 5DD, United Kingdom*

²*Dipartimento di Matematica e Fisica, Università Roma Tre, 00146 Rome, Italy*

³*Bioinformatics Institute, Agency for Science, Technology and Research (A*STAR), Singapore 138671, Singapore*

When graphene is placed on a monolayer of semiconducting transition metal dichalcogenide (TMD) its band structure develops rich spin textures due to proximity spin-orbital effects with interfacial breaking of inversion symmetry. In this work, we show that the characteristic spin winding of low-energy states in graphene on TMD monolayer enables current-driven spin polarization, a phenomenon known as the inverse spin galvanic effect (ISGE). By introducing a proper figure of merit, we quantify the efficiency of charge-to-spin conversion and show it is close to unity when the Fermi level approaches the spin minority band. Remarkably, at high electronic density, even though sub-bands with opposite spin helicities are occupied, the efficiency decays only algebraically. The giant ISGE predicted for graphene on TMD monolayers is robust against disorder and remains large at room temperature.

In the past decade, graphene has emerged as a strong contender for next-generation spintronic devices due to its long spin diffusion lengths at room temperature and gate tunable spin transport [1]. However, the lack of a band gap and its weak spin-orbit coupling (SOC) pose major limitations for injection and control of spin currents. In this regard, van der Waals heterostructures [2] built from stacks of graphene and other two-dimensional (2D) materials hold great promise [3]. The widely tunable electronic properties in vertically-stacked 2D crystals offer a practical route to overcome the weaknesses of graphene [4]. An ideal match to graphene are group-VI dichalcogenides MX_2 (e.g., $M = \text{Mo, W}$; $X = \text{S, Se}$). The lack of inversion symmetry in TMD monolayers enable spin- and valley-selective light absorption [5], thus providing all-optical methods for manipulation of internal degrees of freedom [6]. The optical injection of spin currents across graphene-TMD interfaces has been recently reported [7, 8], following a theoretical proposal [9]. Furthermore, electronic structure calculations show that spin-orbital effects in graphene on TMD are greatly enhanced [10, 11], consistently with the SOC fingerprints in transport measurements [11–14], pointing to Rashba-Bychkov (RB) SOC in the range of 1–10 meV.

In this Letter, we show that the SOC enhancement in graphene on a TMD monolayer allows for current-induced spin polarization, a relativistic transport phenomenon commonly known as ISGE or the Edelstein effect [15]. In the search for novel spintronic materials, the role of the ISGE, together with its Onsager reciprocal—the spin-galvanic effect—is gaining strength, with experimental reports in spin-split 2D electron gases formed in Bi/Ag and $\text{LaAlO}_3/\text{SrTiO}_3$, as well as in topological insulator (TI) $\alpha\text{-Sn}$ thin films [16–18]. In addition, the enhancement of non-equilibrium spin polarization has been proposed in ferromagnetic TMD and magnetically-doped TI/graphene [19]. The robust ISGE in nonmagnetic graphene/TMD heterostructures predicted here promises unique advantages for low-power charge-to-spin conversion (CSC), including the tuning

of spin polarization by a gate voltage. Moreover, owing to the Dirac character of interfacial states in graphene on TMD monolayer, the ISGE shows striking similarities to CSC mediated by ideal topologically protected surface states [20], allowing nearly optimal CSC. We quantify the CSC efficiency as function of the scattering strength, and show it can be as great as $\approx 30\%$ at room temperature (for typical spin-orbit energy scale smaller than $k_B T$).

The model.—The electronic structure of graphene on a TMD monolayer (G/TMD) is well described at low energies by a Dirac model in two spatial dimensions [10, 11]

$$H_{0\mathbf{k}} = \tau_z [v \boldsymbol{\sigma} \cdot \mathbf{k} + \lambda (\boldsymbol{\sigma} \times \mathbf{s}) \cdot \hat{z} + \Delta \sigma_z + \lambda_{\text{sv}} s_z], \quad (1)$$

where $\mathbf{k} = (k_x, k_y)$ is the 2D wavevector around a Dirac point, v is the Fermi velocity of massless Dirac electrons ($v \approx 10^6$ m/s) and σ_i, s_i, τ_i ($i = x, y, z$) are Pauli matrices associated with the sublattice, spin, and valley subspaces, respectively. The momentum-independent terms in Eq. (1) describe a RB effect resulting from interfacial breaking of inversion symmetry (λ), and staggered (Δ) and spin-valley (λ_{sv}) interactions due to broken sublattice symmetry $C_{6v} \rightarrow C_{3v}$ [see Fig. 1 (a)]. The Dirac Hamiltonian $H_{0\mathbf{k}}$ contains all substrate-induced terms (to lowest order in \mathbf{k}) that are compatible with time-reversal symmetry and the point group C_{3v} [21], except for a Kane-Mele SOC term ($\propto \sigma_z s_z$), which is too weak [22, 23] to manifest in transport and can be safely neglected. The dispersion relation associated with $H_{0\mathbf{k}}$ for each valley $\tau \equiv \tau_z = \pm 1$ consists of two pairs of spin split Dirac bands (omitting \hbar)

$$\epsilon_{\tau\zeta}(k) = \pm\tau \sqrt{v^2 k^2 + \Delta_\zeta^2(k)}, \quad (2)$$

where $k \equiv |\mathbf{k}|$, $\zeta = \pm 1$ is the spin-helicity index and

$$\begin{aligned} \Delta_\zeta^2(k) &= \Delta^2 + \lambda_{\text{sv}}^2 + 2\lambda^2 \\ &+ 2\zeta \sqrt{(\lambda^2 - \Delta\lambda_{\text{sv}})^2 + v^2 k^2 (\lambda^2 + \lambda_{\text{sv}}^2)}. \end{aligned} \quad (3)$$

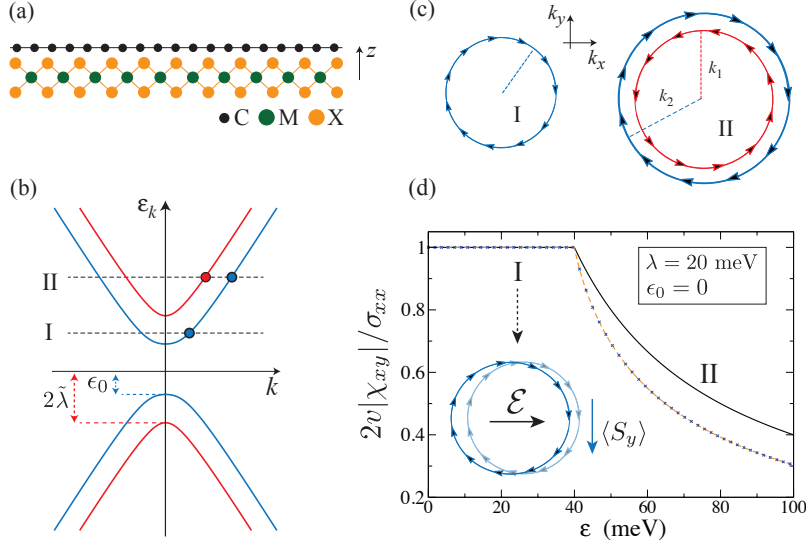


Figure 1. (a) Graphene on a MX_2 monolayer. (b) Typical band structure with spin-split bands with opposite spin helicity. (c) Tangential winding of spin texture in regimes I and II. (d) Ratio between the static spin-charge susceptibility and charge conductivity (in units of $2v$) [thick line (Born limit); dashed line (strong scattering limit, $u_0 \rightarrow \infty$)].

A typical spectrum is shown in Fig. 1(b). The spin texture associated with each band reads

$$\langle \mathbf{s} \rangle_{\alpha \mathbf{k}} = -\zeta \varrho(k) (\hat{k} \times \hat{z}) + m_{\alpha}^z(k) \hat{z}, \quad (4)$$

where $\alpha \equiv (\tau\zeta)$. The first term describes the spin winding generated by the RB effect [Fig. 1(c)] and the second its out-of-plane tilting due to the broken sublattice symmetry. The entanglement between spin and sublattice degrees of freedom generates a nontrivial k dependence in the spin texture. For example, in the minimal model with only RB interaction, $\varrho(k)$ coincides with the band velocity (in units of v), while $m_{\alpha}^z = 0$, i.e., the spin texture is fully in plane [24]. When all interactions in Eq. (1) are included, we find

$$\varrho(k) = \frac{vk\lambda}{\sqrt{(\Delta\lambda_{\text{sv}} - \lambda^2)^2 + v^2k^2(\lambda^2 + \lambda_{\text{sv}}^2)}}. \quad (5)$$

The breaking of sublattice symmetry modifies the spin texture, with both valleys acquiring a spin polarization in the \hat{z} direction, consistently with first-principles studies [10]. The explicit form of $m_{\alpha}^z(k)$ is too cumbersome to be presented. Here, it is sufficient to note that $|m_{\alpha}^z(k=0)| = 1$, with $|m_{\alpha}^z(k)|$ decaying to zero away from the Dirac point [25]. Finally, due to time-reversal symmetry the \hat{z} polarizations at inequivalent valleys are opposite. For energies within the Rashba pseudo gap (RPG), that is, $\epsilon_0 \equiv |\epsilon_{\tau-}(0)| < |\epsilon| < 2\tilde{\lambda} \equiv |\epsilon_{\tau+}(0)|$, the Fermi surface is simply connected. Hence, at low energies, the electronic states have *well-defined spin helicity* [Fig. 1(b-c)]. This feature of G/TMD interfacial states is reminiscent of spin-momentum locking in topologically protected surface states [20], hinting at efficient CSC.

Semiclassical argument.—The efficiency of CSC can be demonstrated using a simple semiclassical argument.

For ease of notation, hereafter we employ natural units ($e \equiv 1 \equiv \hbar$). Under a dc electric field, say $\vec{\mathcal{E}} = \mathcal{E} \hat{x}$, the \hat{y} -polarization spin density in the steady state reads $\langle S_y \rangle = \sum_{\alpha} \int (d\mathbf{k}) \frac{1}{2} \langle s_y \rangle_{\alpha \mathbf{k}} \delta f_{\alpha \mathbf{k}}$, where $\delta f_{\alpha \mathbf{k}}$ is the deviation of the quasiparticle distribution function with respect to equilibrium and $(d\mathbf{k}) \equiv d^2\mathbf{k}/4\pi^2$. Owing to the tangential winding of the in-plane spin texture, only the longitudinal component of the quasiparticle distribution function $\delta f_{\alpha \mathbf{k}}^{\parallel} \equiv g_{\alpha}(k) \hat{k} \cdot \hat{k}_x$ contributes to the integral. At zero temperature, $g_{\alpha}(k) = \mp \mathcal{E} v_{\alpha k} \tau_{* \alpha k} \delta(\epsilon_{\alpha}(k) - \epsilon)$, where $v_{\alpha k} = \partial_k \epsilon_{\alpha}(k)$ is the band velocity, $\tau_{* \alpha k}$ is the longitudinal transport time and ϵ is the Fermi energy (\mp for electron/holes). For energies inside the RPG (regime I), one easily finds

$$\langle S_y \rangle_{\text{I}} = \mp \frac{\mathcal{E}}{4\pi} \varrho(k_F) k_F \tau_*, \quad (6)$$

where k_F is the Fermi momentum and $\tau_* = \tau_*(\tau_-)_{k_F}$ (assumed valley-independent for simplicity). The charge current density, $\langle J_x \rangle = -v \sum_{\alpha} \int (d\mathbf{k}) \langle \tau_z \sigma_x \rangle_{\alpha \mathbf{k}} \delta f_{\alpha \mathbf{k}}$, can be computed following identical steps. We obtain

$$\langle J_x \rangle_{\text{I}} = \frac{\mathcal{E}}{2\pi} v_F k_F \tau_*, \quad (7)$$

where $v_F = |v_{\tau-}(k_F)|$. The implications of our results are best illustrated by considering the minimal model, for which $\varrho(k_F) = v_F/v$ and thus $\langle S_y \rangle_{\text{I}} = \mp \langle J_x \rangle_{\text{I}} / (2v)$. Figure 1(d) shows the ratio of $\langle S_y \rangle / \langle J_x \rangle$ in the linear response regime computed according to the Kubo formula, confirming the linear proportionality $\langle S_y \rangle_{\text{I}} \propto \langle J_x \rangle_{\text{I}}$. The well-defined spin winding direction in regime I, responsible for the semiclassical form of the non-equilibrium spin polarization [Eq. (6)], automatically implies a large ISGE in the clean limit. Generally, the CSC is optimal

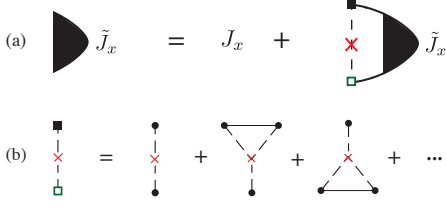


Figure 2. Diagrammatic expansion of the response function. (a) Bethe-Salpeter equation for the charge current vertex in the R - A sector. (b) Skeleton expansion of the T -matrix ladder. Full (open) square denotes a T (T^\dagger) matrix insertion, while circles represent electron-impurity interaction vertices. The red \times stands for impurity density insertion (n).

near the RPG edges, where $|\rho|$ is the largest in regime I. In this energy range, the CSC is *only limited by the electronic mobility*, i.e., $|\langle S_y \rangle|_I \approx \langle J_x \rangle_I / (2v_F) \propto (k_F \tau_*) \mathcal{E}$. These considerations show that $|\rho| \equiv |\langle S_y \rangle| / (2v_F \langle J_x \rangle)$ is the proper figure of merit in regime I. For models with $|\lambda_{sv}| \ll |\lambda|$, the efficiency is *nearly saturated*

$$\max_{\epsilon \in I; \lambda_{sv}=0} |\rho(k(\epsilon))| = 2\sqrt{2}/3 \approx 0.94, \quad (8)$$

and is generally close to unity for not too large spin-valley coupling [25]. In regime II, both spin helicities $\zeta = \pm 1$ contribute to the non-equilibrium spin density, resulting into a decay of the CSC rate. Here, $|\rho|$ is not a suitable figure of merit and an alternative must be sought. As we show later, in this regime ($|\epsilon| > 2\tilde{\lambda}$) the CSC efficiency exhibits an algebraic decay law, enabling a remarkably robust ISGE in typical experimental conditions.

Quantum treatment. — To evaluate the full energy dependence of the ISGE, we employ the self-consistent diagrammatic approach developed by two of us in Ref. [28]. Despite the complexity of the Hamiltonian, Eq. (1), one can solve the Bethe-Salpeter equations for the T -matrix ladder. This provides accurate results in the regime $k_F v_F \tau_* \gg 1$. The zero-temperature spin density-charge current response function reads as

$$\chi_{yx}(\omega = 0) = \frac{1}{2\pi\Omega} \langle \text{Tr} [S_y G^+ J_x G^-] \rangle, \quad (9)$$

where $G^\pm = (\epsilon - H \pm i0^+)^{-1}$ is the Green's function in the retarded/advanced sector of disordered G/TMD. Here, Tr denotes the trace over internal and motional degrees of freedom, $\langle \dots \rangle$ stands for disorder average and Ω is the area. In the diagrammatic approach, the disorder enters as a self-energy, Σ^a ($a = \pm$), “dressing” the single-particle Green's functions, and as vertex corrections in the electron-hole propagator [Fig. 2 (a)]. Since the response functions of interest are determined by the same relaxation time, τ_* , the CSC is expected to be little sensitive to the disorder type as long as the latter is non magnetic. For practical purposes, we use a model of short-range scalar impurities, $V(\mathbf{x}) = u_0 \sum_{i=1}^N \delta(\mathbf{x} - \mathbf{x}_i)$, where $\{\mathbf{x}_i = (x_i, y_i)\}$ are random impurity locations and u_0 parametrizes their strength. This choice will enable us to establish key analytical results across weak (Born) and strong (unitary) scattering regimes.

We first evaluate Eq. (9) for models with fully in-plane spin texture, $\Delta, \lambda_{sv} = 0$. For ease of notation, we assume $\epsilon, \lambda > 0$ in what follows. The self-energy is given by $\Sigma^a = n T^a$, where $T^a = (u_0^{-1} \mathbb{1} - g_0^a)^{-1}$ and $n = N/\Omega$ is the impurity areal density. Moreover, $g_0^a \equiv \int (d\mathbf{k}) G_{0\mathbf{k}}^a$ and $G_{0\mathbf{k}}^\pm = (\epsilon - H_{0\mathbf{k}} \pm i0^+)^{-1}$ is the bare Green's function. Neglecting the real part of Σ^a , we have

$$\Sigma^\pm = \mp i n (\eta_0 \gamma_0 + \eta_3 \gamma_{\text{KM}} + \eta_r \gamma_r), \quad (10)$$

where $\gamma_0 = \tau_0 \sigma_0 s_0$ (identity), $\gamma_r = \tau_z (\boldsymbol{\sigma} \times \mathbf{s}) \cdot \hat{z}$, $\gamma_{\text{KM}} = \tau_0 \sigma_z s_z$ and in the weak scattering limit

$$\eta_0 = \frac{u_0^2}{8v^2} (\epsilon + \lambda), \quad \eta_3 = \frac{u_0^2}{8v^2} \lambda, \quad \eta_r = -\frac{u_0^2}{16v^2} \epsilon, \quad (11)$$

inside the RPG and $\eta_0 = u_0^2 \epsilon / 4v^2$ and $\eta_{\text{KM}} = \eta_r = 0$ for $\epsilon > 2\lambda$ (see [25] for full T -matrix expressions). The rich matrix structure in Eq. (10) stems from the chiral (pseudo-spin) character of quasiparticles. In contrast, in the 2D electron gas with RB spin-orbit interaction, the self energy due to spin-independent impurities is a scalar in all regimes [29]. Next, we evaluate the disorder averaged Green's function, $G_{\mathbf{k}}^a = [(G_{0\mathbf{k}}^a)^{-1} - \Sigma^a]^{-1}$. We define $\epsilon^a = \epsilon + i a n \eta_0$, $\lambda^a = \lambda - i a n \eta_r$, and $m^a = i a n \eta_3$, which represent an energy shift, a renormalized RB coupling and a random SOC gap, respectively. After tedious but straightforward algebra we find

$$G_{\mathbf{k}}^a = - \left[(\epsilon^a L_+^a + \lambda^a L_-^a) \gamma_0 + v L_+^a \tau_z \boldsymbol{\sigma} \cdot \mathbf{k} - \frac{1}{2} (\epsilon^a - m^a) L_-^a \gamma_r + (m^a L_+^a + \lambda^a L_-^a) \gamma_{\text{KM}} - v L_-^a \gamma_{v\mathbf{k}} + \Gamma_{\mathbf{k}}^a \right], \quad (12)$$

where $L_\pm^a = (L_1^a \pm L_2^a)/2$ with

$$L_{1(2)}^a = [v^2 k^2 - (\epsilon^a - m^a)(\epsilon^a + m^a \pm 2\lambda^a)]^{-1}, \quad (13)$$

$\gamma_{v\mathbf{k}} = \tau_0 \sigma_0 (\hat{\mathbf{k}} \times \mathbf{s}) \cdot \hat{z}$ and $\Gamma_{\mathbf{k}}^a$ is a k_i -quadratic term [25].

The last step consists of evaluating the vertex corrections. The renormalized charge current vertex satisfies

the Bethe-Salpeter (BS) equation

$$\tilde{J}_x = J_x + n \int (d\mathbf{k}) \{ T^+ \mathcal{G}_\mathbf{k}^+ \tilde{J}_x \mathcal{G}_\mathbf{k}^- T^- \}. \quad (14)$$

The infinite set of non-crossing diagrams generated by the T -matrix ladder describes incoherent multiple scattering events *at all orders* in the scattering strength u_0 [Fig. 2(b)], yielding an accurate description of spin-orbit coupled transport phenomena in the dilute regime [28]. To solve Eq. (14), we decompose \tilde{J}_x as $\tilde{J}_x = \tilde{J}_x^{\mu\nu\rho} \tau_\mu \sigma_\nu s_\rho$, where the repeated indices $\mu, \nu, \rho \equiv \{0, i\}$ are summed over. The number of nonzero components $\tilde{J}_x^{\mu\nu\rho}$ is constrained to only four by the symmetries of G/TMD [30]: $(\mu, \nu, \rho) = \{(0, 0, y), (z, x, 0), (0, z, x), (z, y, z)\}$. Exploring the properties of the Clifford algebra, one can show that the nonzero vertex components have a one-to-one correspondence to their associated non-equilibrium response functions [31]. This allows us to express χ_{yx} in terms of the spin density component *only*, $\tilde{J}_x^s \equiv \tilde{J}_x^{00y}$, i.e., $\chi_{yx} = F_s(u_0) \tilde{J}_x^s$, where

$$\tilde{J}_x^s = -\frac{v}{\epsilon} \frac{\epsilon^2 (\epsilon + 2\lambda) + \theta(\epsilon - 2\lambda) (8\lambda^3 - \epsilon^3)}{\epsilon^2 + 4\lambda^2} + \varepsilon_\Lambda. \quad (15)$$

Here, θ is the Heaviside step function and ε_Λ is a weak correction logarithmic in the ultraviolet cutoff Λ set by the inverse of the lattice scale [32]. Finally, $F_s(u_0)$ is a complicated function, which in the Gaussian and unitary scattering limits takes the form

$$F_s(u_0) = \frac{1}{2\pi n} \times \begin{cases} \frac{4}{u_0^2} & , |g_0^+ u_0| \ll 1 \\ \left(\frac{\epsilon}{2\pi v^2} \log \left| \frac{\Lambda^2}{\epsilon\sqrt{\epsilon^2 - 4\lambda^2}} \right| \right)^2 & , |u_0| \rightarrow \infty \end{cases}, \quad (16)$$

respectively. Analogously, we can determine the expression for the charge conductivity $\sigma_{xx} = F_c(u_0) \tilde{J}_x^c$, with $\tilde{J}_x^c \equiv \tilde{J}_x^{zx0}$ [25]. The CSC rate can now be determined

$$-\frac{2v\chi_{yx}}{\sigma_{xx}} = \theta(2\lambda - \epsilon) + \frac{2\lambda}{\epsilon} g(u_0, \epsilon) \theta(\epsilon - 2\lambda), \quad (17)$$

where $g(u_0, \epsilon = 2\lambda) = 1$ and deviates only slightly from this value when u_0 is large and for $\epsilon > 2\lambda$ [see Fig. 1(d)]. The central result Eq. (17) puts our earlier semiclassical argument on firm grounds, and shows that the CSC is little affected by the disorder strength outside the RPG.

Discussions.— In realistic G/TMD heterostructures, Δ and λ_{sv} can be comparable to the RB coupling [10], leading to major modifications in the band structure. Nevertheless, a thorough analysis, summarized in Fig. 3, shows that the ISGE remains robust. For instance, for $|\lambda_{sv}| \ll \lambda, |\Delta|$, the k dependence of the in-plane spin texture is virtually unaffected [Eq. (5)]. Thus, according to the semiclassical results the CSC efficiency should be high at the RPG edge. This is confirmed by a numerical inversion of the Bethe-Salpeter equations in the full model. The figure of merit γ plotted in Fig. 3 reaches its predicted optimal value [Eq. (8)]. When the spin-valley

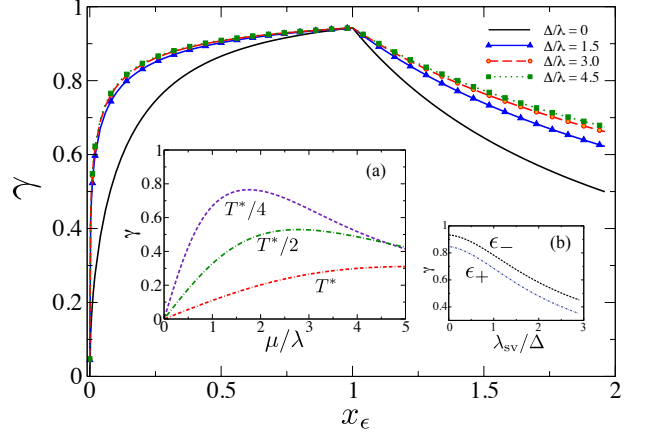


Figure 3. Main figure: Fermi energy dependence of the ISGE efficiency at selected values of Δ for $\lambda = 15$ meV and $\lambda_{sv} = 0$. The x -axis is rescaled as $x_\epsilon = |\epsilon - \epsilon_0| / |2\tilde{\lambda} - \epsilon_0|$ for clarity. Inset: (a) γ as function of chemical potential (μ) at selected temperatures for a prototypical heterostructure with $\lambda = 10$ meV, $\lambda_{sv} = \Delta = 0$ (Ref. [13]); $k_B T^* = 25$ meV (room temperature). (b) Variation of γ with λ_{sv} for a Fermi energy slightly below (above) the RPG's edge [$\epsilon_\pm = 2\tilde{\lambda} \times (1.00 \pm 0.05)$] for $\Delta = \lambda/2$ and $\lambda = 15$ meV. All calculations performed in the weak scattering limit.

coupling is significant, the in-plane spin texture shrinks, however the CSC efficiency remains sizeable [Fig. 3(b)]. Outside the RPG, the definition of efficiency γ is complicated due to the coexistence of counter-rotating spins. To analyze this regime, we employ a heuristic definition satisfying: (i) $0 \leq \gamma \leq 1$ for all parameters, (ii) γ decays for $\epsilon \gg 2\tilde{\lambda}$ due to collapsing of spin-split Fermi rings and (iii) γ is continuous across the RPG. Since the band velocity saturates quickly to its upper bound ($= v$), we use its value at the RPG edge as representative for the regime II, which lead us to the following definition

$$\gamma = \frac{2|\chi_{yx}|}{\sigma_{xx}} \times \begin{cases} v_F(\epsilon) & , \epsilon < 2\tilde{\lambda} \\ v_F(2\tilde{\lambda}) & , \epsilon \geq 2\tilde{\lambda} \end{cases}. \quad (18)$$

where $v_F(\epsilon) \equiv |v_{\tau-}(k(\epsilon))|$. Consistently with the rate derived for the minimal model [Eq. (17)], the asymptotic behavior of γ is of power-law type, and thus the CSC remains robust in the accessible range of electronic densities. A relevant question is how much efficiency is lost due to thermal fluctuations. Figure 3(b) shows the CSC figure of merit at selected temperatures in the weak scattering limit (see Ref. [25] for methods). Since the $T = 0$ ratio decays slowly in regime II, the smearing caused by thermal activation is ineffective, allowing a giant ISGE at room temperature, e.g., $\gamma_{\text{room}} \approx 0.3$ for a chemical potential $\mu \approx 5\lambda \approx 50$ meV. We finally comment on the rippling of the graphene surface and imperfections causing local variations in the RPG [33]. Inhomogeneities in the spin-orbit energy scales are expected to be small in samples with strong interfacial effect [34]. As long as

$|\lambda(\mathbf{x}) - \lambda| \ll \lambda$, the random spin-orbit field acts merely as an additional source of scattering [25], which according to our findings would not affect the ISGE efficiency.

In conclusion, we have presented a rigorous theory of inverse spin galvanic effect for graphene on transition metal dichalcogenide monolayers. We introduced a figure of merit for charge-to-spin conversion and show it attains values close to unity at the minority spin band edge. The effect is robust against nonmagnetic disorder and remains large at room temperature. The current-driven spin polarization is only limited by the electronic mobility, and thus it is expected to achieve unprecedentedly large values in ultra-clean samples. Our results are also relevant for group-IV honeycomb layers [35], which are described by similar Dirac models.

The codes used for numerical analyses are available from the Figshare database, under the Ref [36].

M.M. thanks C. Verma for his hospitality at the Bioinformatics Institute in Singapore. A.F. gratefully acknowledges the financial support from the Royal Society (U.K.) through a Royal Society University Research Fellowship. R.R. acknowledges the hospitality of CA2DM at NUS under grant R-723-000-009-281 (GL 769105). M.O. and A.F. acknowledge funding from EP-SRC (Grant Ref: EP/N004817/1).

* milletari@gmail.com

† aires.ferreira@york.ac.uk

- [1] W. Han, R.K. Kawakami, M. Gmitra, and J. Fabian. *Nature Nano.* **9**, 794 (2014).
- [2] A. K. Geim, and I. V. Grigorieva. *Nature* **499**, 419 (2013).
- [3] A. Soumyanarayanan, N. Reyren, A. Fert, and C. Panagopoulos. *Nature* **539**, 509 (2016).
- [4] L. Britnell, *et al.* *Science* **340**, 1311 (2013). A. V. Kretinin, *et al.* *Nano Lett.* **14** (2014); H. Fang, *et al.* *PNAS* **111**, 6198 (2014); F. Withers, *et al.* *Nat. Materials*, **14** 301 (2015). T. Shen, A.V. Penumatcha, and J. Appenzeller, *ACS Nano* **10**, 4712 (2016).
- [5] Z. Zhu *et al.* *Physical Review B*, **84**, 153402 (2011); D. Xiao, *et al.* *Physical Review Letters* **108**, 196802 (2012); K. F. Mak, *et al.* *Nature Nanotechnology* **7**, 494 (2012); H. Zeng *et al.* *Nature Nanotechnology* **7**, 490-493 (2012).
- [6] R.A. Muniz, and J.E. Sipe, *Phys. Rev. B* **91**, 85404 (2015).
- [7] Y.K. Luo *et al.* *Nanoletters* **17**, 3877 (2017);
- [8] A. Avsar *et al.* pre-print: arXiv:1705.10267 (2017).
- [9] M. Gmitra, J. Fabian, *Physical Review B*, **92**, 155402 (2015).
- [10] M. Gmitra, D. Kochan, P. Högl, and J. Fabian, *Phys. Rev. B* **93**, 155104 (2016).
- [11] Z. Wang, *et al.* *Nature Communications* **6**, 8339 (2015).
- [12] A. Avsar, *et al.* *Nature Communications* **5**, 4875 (2014).
- [13] Z. Wang, *et al.* *Phys. Rev. X* **6**, 041020 (2016).
- [14] T. Völkl, *et al.* pre-print: arXiv:1706.07189 (2017).
- [15] E. I. Rashba, *Sov. Phys. Solid State* **2**, 1109 (1960); E. L. Ivchenko and G. E. Pikus, *JETP Lett.* **27**, 604 (1978); E. L. Ivchenko, Y. B. Lyanda-Geller, and G. E. Pikus, *JETP Lett.* **50**, 175 (1989); A. G. Aronov and Y. B. Lyanda-Geller, *JETP Lett.* **50**, 431 (1989). V. M. Edelstein, *Solid State Comm.* **73**, 233 (1990).
- [16] J. R. Sánchez, *et al.* *Nature Comm.* **4**, 2944 (2013).
- [17] J. R. Sánchez, *et al.* *Phys. Rev. Lett.* **116**, 096602 (2016).
- [18] E. Lesne, *et al.* *Nature Materials* **15**, 1261-1266 (2016).
- [19] M. Rodriguez-Vega, G. Schwiete, J. Sinova, and E. Rossi, pre-print: arXiv:1610.04229 (2016). X. Li, H. Chen, and Q. Niu, pre-print: arXiv:1707.04548 (2017).
- [20] P. Schwab, R. Raimondi, and C. Gorini. *EPL* **93**, 67004 (2011).
- [21] D. Kochan, S. Irmer, and J. Fabian. *Phys. Rev. B* **95**, 165415 (2017).
- [22] D. Huertas-Hernando, F. Guinea, and A. Brataas, *Phys. Rev. B* **74**, 155426 (2006).
- [23] S. Konschuh, M. Gmitra, and J. Fabian, *Phys. Rev. B* **82**, 245412 (2010).
- [24] E. I. Rashba, *Physical Review B* **79**, 161409 (2009).
- [25] See Supplemental Material attached below for explicit expressions and further discussions. Additional Refs. [26, 27] are also included therein.
- [26] M. A. H. Vozmediano, *Philos. Trans. R. Soc., A* **369**, 2625 (2011).
- [27] C. Huang, Y.D. Chong, M. A. Cazalilla. *Phys. Rev. B* **94**, 085414 (2016).
- [28] M. Milletari and A. Ferreira, *Phys. Rev. B* **94**, 134202 (2016); *ibidem*, 201402 (2016).
- [29] P. Schwab and R. Raimondi, *EPJ B* **25**, 483 (2002).
- [30] Invariance under mirror reflection about \hat{x} -axis and isospin rotations, $\Lambda_z = \tau_z$, reduces Eq. (14) to a set of 8×8 coupled equations. In addition, the minimal Dirac-Rashba model is invariant under a rotation of π exchanging sublattices, C_2 , and $\Lambda_{x,y} = \tau_{x,y}\sigma_z$, leading to only four allowed components.
- [31] M. Milletari, M. Offidani, A. Ferreira, and R. Raimondi, *Phys. Rev. Lett.* **119**, 246801 (2017).
- [32] A. Ferreira, J. Viana-Gomes, J. Nilsson, E. R. Mucciolo, N. Peres, and A. C. Neto, *Phys. Rev. B* **83**, 165402 (2011).
- [33] M. B. Lundeberg, and J. A. Folk. *Phys. Rev. Lett.* **105**, 146804 (2010); V. K. Dugaev, E. Y. Sherman, and J. Barnaś. *Phys. Rev. B* **83**, 085306 (2011); I. M. Vicent, H. Ochoa, and F. Guinea. *Phys. Rev. B* **95**, 195402 (2017)
- [34] B. Yang, *et al.* *Phys. Rev. B* **96**, 041409(R) (2017).
- [35] S. Cahangirov, *et al.*, *Phys. Rev. Lett.* **102**, 236804 (2009). T. Amlaki, M. Bokdam, and P. J. Kelly. *Phys. Rev. Lett.* **116**, 256805 (2009). C.-C. Liu, H. Jiang, and Y. Yao, *Phys. Rev. B* **84**, 195430 (2011).
- [36] DOI: <https://doi.org/10.6084/m9.figshare.c.3904732.v1>.

SUPPLEMENTARY INFORMATION FOR “OPTIMAL CHARGE-TO-SPIN CONVERSION IN GRAPHENE ON TRANSITION METAL DICALCOGENIDES”

In this Supplementary Information we provide additional details on the Dirac-Rashba model and the semiclassical theory at large electronic density. We also provide the explicit form of the renormalized charge current vertex for the minimal model (i.e., $\Delta = \lambda_{sv} = 0$, $\lambda \neq 0$), as well as additional details on the finite temperature calculation and the impact of random fluctuations in the spin-orbit energy scale.

I. DETAILS ON THE MODEL

A. Spectrum

The effective Hamiltonian of graphene on TMD monolayer can be written as [10, 11]

$$H_{0\mathbf{k}} = \tau_z [v \boldsymbol{\sigma} \cdot \mathbf{k} + \lambda (\boldsymbol{\sigma} \times \mathbf{s}) \cdot \hat{z} + \Delta \sigma_z + \lambda_{sv} s_z], \quad (19)$$

where $\boldsymbol{\sigma}, \mathbf{s}$ are Pauli matrices and we have used the representation for the 4-component spinors at each valley ($\tau_z = \pm 1$):

$$\psi_{\tau_z = \pm} = (\psi_{\pm, a(b)}^\uparrow, \psi_{\pm, a(b)}^\downarrow, \psi_{\pm, b(a)}^\uparrow, \psi_{\pm, b(a)}^\downarrow)^t. \quad (20)$$

In the above, $a(b)$ are graphene sublattice indexes, and \uparrow, \downarrow denote the spin projection. The respective eigenvalues are given in Eqs. (2)-(3) of main text. The Rashba pseudo-gap at $k = 0$ (see Fig. 1, main text) is easily computed as

$$2\tilde{\lambda} = \min\{|\Delta + \lambda_{sv}|, \sqrt{4\lambda^2 + (\Delta - \lambda_{sv})^2}\}, \quad (21)$$

while the bottom of the spin majority conduction band is

$$\epsilon_m = \frac{|\lambda(\Delta + \lambda_{sv})|}{\sqrt{\lambda^2 + \lambda_{sv}^2}}. \quad (22)$$

For energies $\epsilon_m < \epsilon < 2\tilde{\lambda}$ the spectrum develops a small “Mexican hat” feature [10]. In Fig. 4 we show the evolution of the spectrum for finite Rashba effect as one turns on the proximity couplings Δ, λ_{sv} . We note that the energy spectrum is gapless in the following particular cases: (i) $\lambda = 0$ and $|\lambda_{sv}| > |\Delta|$ and (ii) $\lambda_{sv} = -\Delta$.

In the minimal model ($\Delta, \lambda_{sv} = 0$) the spin texture is entirely in-plane, due to the Rashba spin-momentum locking. The additional proximity-induced couplings in Eq. (19) favor the establishment of a finite s_z -component. In Fig. 5, we show the spin texture of the electron spin-majority band for a number of representative cases.

B. Semiclassical interpretation of the large energy behavior of the spin-charge response function

We demonstrate how the asymptotic scaling of the ISGE efficiency reported in the main text [viz., Eq. (17)] can be understood within a simple semiclassical picture. For simplicity we study the pure-Rashba model, where $m\tilde{\zeta}(k) = 0$. The argument can be easily generalized for other cases. Neglecting interband transitions, the spin- y linear response to an electric field applied along \hat{x} axis is given by [cf. Eq. (6) of the main text]

$$\chi_{yx} = \frac{1}{4\pi} \int \frac{d\theta_{\mathbf{k}}}{2\pi} \sum_{\zeta = \pm 1} \langle s_y \rangle_{\zeta} \cos \theta_{\mathbf{k}} k_{\zeta}(\epsilon) \tau_{*\zeta}(\epsilon) \quad (23)$$

where $k_{\zeta}(\epsilon) = v^{-1} \sqrt{\epsilon(\epsilon - \zeta\lambda)}$ are the Fermi radii. Substituting the expression for the equilibrium spin texture [Eq. (5); main text], we find, for large ϵ

$$\chi_{yx} \simeq -\frac{1}{8\pi} \sum_{\zeta = \pm 1} \zeta \frac{\epsilon}{v} \left(1 - \zeta \frac{\lambda}{2\epsilon} + \dots \right) \tau_{*\zeta}(\epsilon). \quad (24)$$

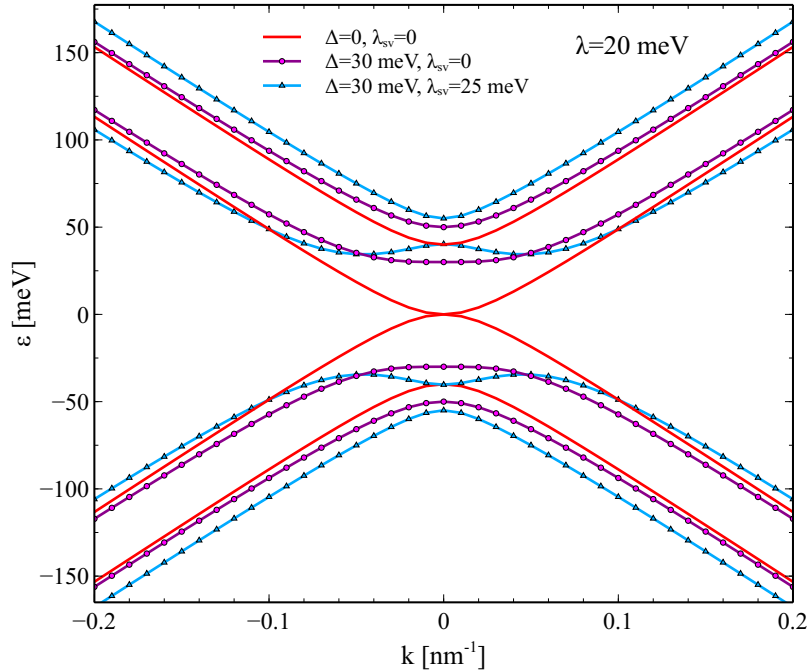


Figure 4. Spectrum of the full model. For $\Delta = 0, \lambda_{sv} = 0$ (solid lines) the spectrum displays a Rashba pseudogap, with a simply connected Fermi surface at low energies and no band gap. A finite staggered potential, $\Delta = 30$ meV, opens a gap (circles), which in combination with $\lambda_{sv} = 25$ meV creates a “Mexican hat” between ϵ_m and $\delta/2$ (triangles).

Using the form of the momentum relaxation time in the Gaussian and unitary limits, we find, respectively

$$\tau_{*\zeta}(\epsilon) = A/\epsilon \quad \longrightarrow \quad \chi_{yx} = \frac{A}{8\pi v} \frac{\lambda}{\epsilon}, \quad (25)$$

$$\tau_{*\zeta}(\epsilon) = A'\epsilon \quad \longrightarrow \quad \chi_{yx} = \frac{A'}{8\pi v} \lambda \epsilon. \quad (26)$$

While the collapsing of the Fermi rings, $k_\zeta(\epsilon) \rightarrow k_{-\zeta}(\epsilon)$ as $\epsilon \gg 2|\lambda|$, tends to diminish the out-of-equilibrium spin polarization, the latter can still be finite depending on the asymptotic behavior of $\tau_*(\epsilon)$. In the unitary limit, one has $vk_\zeta(\epsilon)\tau_{*\zeta}(\epsilon) \propto \epsilon^2$, resulting in a monotonically increasing spin-charge response function. However, the ratio between the spin-charge response function and the charge conductivity is always $\chi_{yx}/\sigma_{xx} \propto \epsilon^{-1}$, as shown in the main text. While in Eqs. (25)-(26) we have neglected the role of scattering between states with different spin helicity, the latter processes are included in the quantum-mechanical treatment in the main text. Given the agreement of Eqs. (25)-(26) with Eq. (16) of the main text, we conclude that their inclusion will not affect the above semiclassical picture.

II. DETAILS ON THE DIAGRAMMATIC CALCULATION

A. Disorder averaged propagators

We provide the full form of the disorder averaged propagator in the pure-Rashba model. Denoting with $a = \pm$, respectively, the retarded and advanced sector of the theory, we obtain

$$G_{\mathbf{k}}^a = - \left[(\epsilon^a L_+^a + \lambda^a L_-^a) \gamma_0 + v L_+^a \tau_z \boldsymbol{\sigma} \cdot \mathbf{k} - \frac{1}{2} (\epsilon^a - m^a) L_-^a \gamma_r + (m^a L_+^a + \lambda^a L_-^a) \gamma_{\text{KM}} - v L_-^a \tau_0 \sigma_0 (\hat{\mathbf{k}} \times \mathbf{s}) \cdot \hat{\mathbf{z}} + \Gamma_{\mathbf{k}}^a \right], \quad (27)$$

where

$$\epsilon^a = \epsilon + i a n \eta_0, \quad \lambda^a = \lambda - i a n \eta_r, \quad m^a = -i a n \eta_3, \quad (28)$$

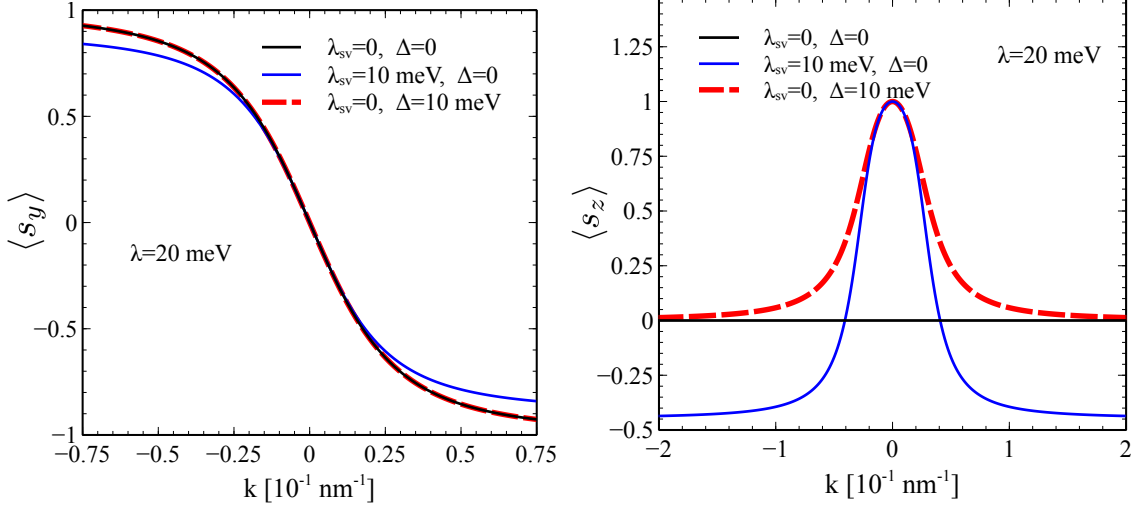


Figure 5. Spin texture for electronic states along \hat{k}_x in the spin-majority conduction band. In the pure Rashba model the spins lie entirely in the plane, $\langle s_z \rangle = 0$. When λ_{sv} or Δ are switched on, electrons develop a $\langle s_z \rangle$ component. Interestingly, for $\Delta \neq 0$ and $\lambda_{\text{sv}} = 0$ the latter does not imply a decrease of $\langle s_y \rangle$ (see left panel).

$$L_{\pm}^a = (L_1^a \pm L_2^a)/2, \quad L_{1(2)}^a = [v^2 k^2 - (\epsilon^a - m^a)(\epsilon^a + m^a \pm 2\lambda^a)]^{-1}, \quad (29)$$

and

$$\Gamma_{\mathbf{k}}^a = \left(\lambda^a L_+^a \tau_0 + \frac{(\epsilon^a + m^a)}{2} L_-^a \tau_z \right) [\sin 2\phi_{\mathbf{k}} (\sigma_x s_x - \sigma_y s_y) - \cos 2\phi_{\mathbf{k}} \tau_z (\sigma_x s_y + \sigma_y s_x)]. \quad (30)$$

B. T -matrix calculation

We report the full form of the imaginary part of the self-energy in the T -matrix approximation:

$$\Sigma^{\pm} = \mp i n (\eta_0 \gamma_0 + \eta_3 \gamma_{\text{KM}} + \eta_r \gamma_r), \quad (31)$$

$$\eta_0, \eta_3 = \frac{u_0}{2} \text{Im} \left[\frac{1}{1 - u_0 (g_{0,0}^+ + g_{0,\text{KM}}^+)} \pm \frac{1 - u_0 (g_{0,0}^+ - g_{0,\text{KM}}^+)}{[1 - u_0 (g_{0,0}^+ - g_{0,\text{KM}}^+)]^2 - (2u_0 g_{0,r}^+)^2} \right], \quad (32)$$

$$\eta_r = \text{Im} \left[\frac{u_0 g_{0,r}^+}{[1 - u_0 (g_{0,0}^+ - g_{0,\text{KM}}^+)]^2 - (2u_0 g_{0,r}^+)^2} \right], \quad (33)$$

with $g_{0,i}^+ = \frac{1}{8} \text{Tr}[g_0^+ \gamma_i]$ and $\gamma_i = \{\gamma_0, \gamma_{\text{KM}}, \frac{1}{2}\gamma_r\}$ as defined in the main text. The real part of the self-energy (omitted for simplicity) leads to a renormalization of the Fermi energy and of λ as well as a random mass term of the Kane-Mele type [28]. The Fermi energy renormalization contains a logarithmic divergence, which can be taken into account by wave function renormalization and leads to a renormalization of the Fermi velocity [26].

C. Full form of the renormalized charge vertex

We first define the general structure of the renormalized charge current vertex in the minimal model as

$$\{\tilde{J}_x^c, \tilde{J}_x^s, \tilde{J}_x^{sh}, \tilde{J}_x^m\} = \frac{1}{8} \text{Tr} [\tilde{J}_x \{\tau_z \sigma_x, s_y, \tau_z \sigma_y s_z, \sigma_z s_x\}]. \quad (34)$$

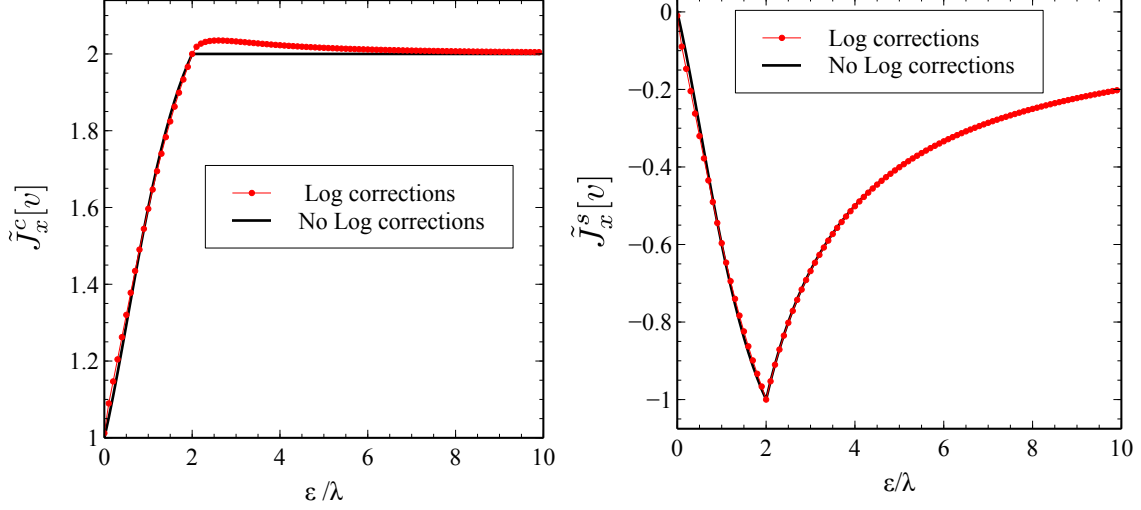


Figure 6. The charge \tilde{J}_x^c and spin density \tilde{J}_x^s component of the renormalized charge vertex for $\lambda = 25$ meV. Corrections logarithmic in the cutoff $\Lambda = 10$ eV are shown to be small.

Below we provide the explicit form of the components to lowest order in the impurity density n for the weak scattering limit. For simplicity, we assume $\lambda > 0$. Outside the Rashba pseudogap, $\epsilon > 2\lambda$, we obtain

$$\tilde{J}_x^c = 2v + \mathcal{O}(n), \quad \tilde{J}_x^s = -\frac{2\lambda}{\epsilon}v + \mathcal{O}(n), \quad \tilde{J}_x^{sh,m} = 0, \quad (35)$$

while inside the Rashba pseudogap, $\epsilon < 2\lambda$, we find

$$\tilde{J}_x^c = v \frac{2(\epsilon^2 + \lambda\epsilon + 2\lambda^2)}{\epsilon^2 + 4\lambda^2} + \mathcal{O}(n), \quad (36)$$

$$\tilde{J}_x^s = -v \frac{\epsilon(\epsilon + 2\lambda)}{\epsilon^2 + 4\lambda^2} + \mathcal{O}(n), \quad (37)$$

$$\tilde{J}_x^{sh} = \frac{n u_0^2 \epsilon}{16 v \lambda} + \mathcal{O}(n^2), \quad (38)$$

$$\tilde{J}_x^m = \frac{n u_0^2 \epsilon^2}{4 v \epsilon^2 + 4\lambda^2} + \mathcal{O}(n^2). \quad (39)$$

At leading order in n , the important components are $\tilde{J}_x^c, \tilde{J}_x^s$. In the strong scattering regime Eqs. (15)-(19) acquire logarithmic corrections in the ultraviolet cutoff Λ . In Fig. 6 we show that such corrections are small for the leading terms \tilde{J}_x^c and \tilde{J}_x^s , so that Eqs. (15)-(17) still hold in this regime. Having performed the limit $u_0 \rightarrow \infty$, Eqs. (18),(19) for the subleading components $\tilde{J}_x^{sh}, \tilde{J}_x^m$ are no longer valid; yet we find the corrections provide a negligible contribution to the response functions (not shown).

D. Finite temperature calculation for the ISGE efficiency

In Fig. (3) of the main text we showed the figure of merit's temperature-dependence. The calculation was performed numerically employing the following definition

$$\gamma(\mu, T) = \frac{\int_{-\infty}^{+\infty} d\epsilon \frac{\partial f(\epsilon, \mu, T)}{\partial \epsilon} 2|\chi_{yx}(\epsilon, T=0)| [\theta(|\epsilon| - 2\tilde{\lambda})v_F(2\tilde{\lambda}) + \theta(2\tilde{\lambda} - |\epsilon|)v_F(\epsilon)]}{\int_{-\infty}^{+\infty} d\epsilon \frac{\partial f(\epsilon, \mu, T)}{\partial \epsilon} \sigma_{xx}(\epsilon, T=0)}, \quad (40)$$

where $f(\epsilon, \mu, T) = \{1 + \exp[(\epsilon - \mu)/k_B T]\}^{-1}$ is the Fermi-Dirac distribution function; see main text for remaining definitions.

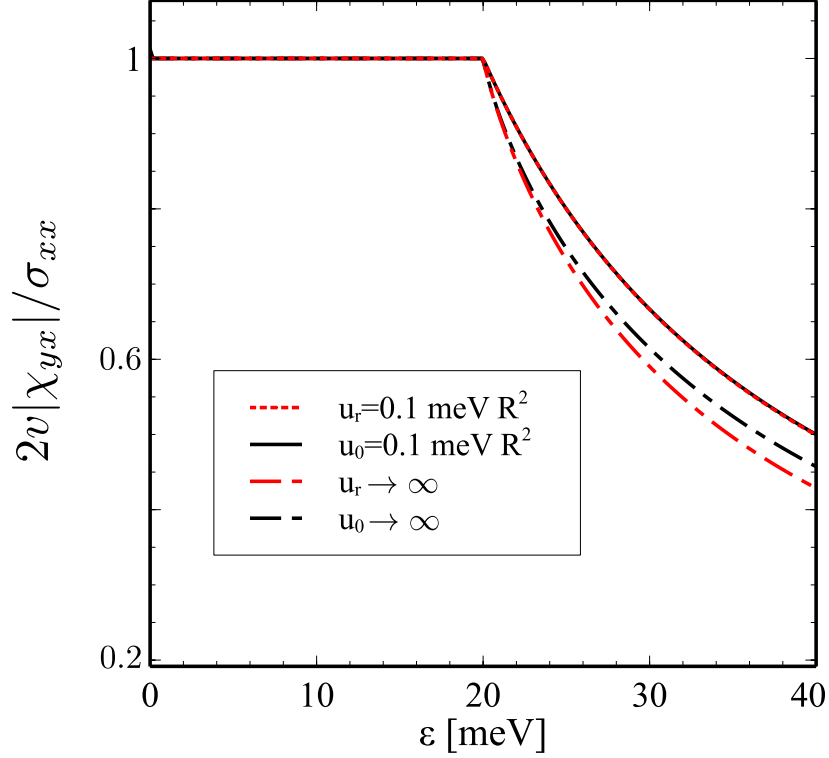


Figure 7. Comparison between pure scalar (u_0) and pure Rashba disorder (u_r). $R = 6$ nm, $\lambda = 10$ meV. While for in the weak scattering limit the results coincide, Rashba impurities have a slightly more important impact in the UL. However the difference between the two cases is clearly very tiny.

III. EFFECT OF RANDOM SOC

We analyze here the impact of *random* Rashba fields (RRFs) on the CSC efficiency. In graphene without proximity SOC, RRFs lead to current-driven spin polarization via asymmetric spin precession [27]. In graphene on TMD, small fluctuations in the Rashba-Bychkov coupling ($|\lambda(\mathbf{x}) - \lambda| \ll \lambda$) cannot disturb the spin helicity of eigenstates. This directly implies that the CSC rate in regime I remains unaffected (see main text). To investigate the impact of random SOC in regime II, we model the RRF as a short-range disorder potential with Rashba-Bychkov matrix structure:

$$V_{\text{RRF}}(\mathbf{x}) = u_r \gamma_r \sum_{i=1}^N \delta(\mathbf{x} - \mathbf{x}_i), \quad (41)$$

Neglecting its real part real, the self-energy Σ^a preserves the structure of Eq. 10 of the main text

$$\Sigma^\pm = \mp i n (\eta_0 \gamma_0 + \eta_3 \gamma_{\text{KM}} + \eta_r \gamma_r), \quad (42)$$

where $\gamma_0 = \tau_0 \sigma_0 s_0$ (identity), $\gamma_r = \tau_z (\boldsymbol{\sigma} \times \mathbf{s}) \cdot \hat{z}$, $\gamma_{\text{KM}} = \tau_0 \sigma_z s_z$. We report the the weak scattering limit form of the parameters appearing in Eq. (42) for positive energies

$$\begin{cases} \eta_0 = -\eta_r = \frac{u_r^2}{2v^2} \epsilon, \quad \eta_r = 0, & \epsilon > 2\lambda \\ \eta_0 = -\eta_r = -\eta_3 = \frac{u_r^2}{4v^2} \epsilon, & \epsilon < 2\lambda \end{cases}. \quad (43)$$

We find that at leading order in the impurity areal density, Eq.(17) of the main text still holds with a slightly different functional form for $g(u_r, \epsilon)$. In Fig. (7) we plot the ratio $|\chi_{yx}|/\sigma_{xx}$ for Rashba-like and scalar impurities (as considered in the main text); the CSC ratio in the two cases is virtually identical in the Born scattering regime. This confirms that as long as the proximity effect is well developed in the band structure of graphene, the CSC mechanism is robust against random fluctuations in the energy scales of the model.